Review of Scientific Instruments

RESEARCH ARTICLE | MARCH 20 2026

# Spectroscopic method for measuring the radial component of the magnetic field in cylindrically imploding plasmas

Marko Cvejić ; Tal Queller ; Eyal Kroupp ; Dimitri Mikitchuk ; Ramy Doron ; Vladimir Bernshtam; Oleg Nedostup ; Amnon Fruchtman ; Yitzhak Maron



*Rev. Sci. Instrum.* 97, 033508 (2026)
https://doi.org/10.1063/5.0301238

Review of Scientific Instruments ARTICLE pubs.aip.org/aip/rsi

# Spectroscopic method for measuring the radial component of the magnetic field in cylindrically imploding plasmas

Cite as: Rev. Sci. Instrum. 97, 033508 (2026); doi: 10.1063/5.0301238
Submitted: 7 September 2025 • Accepted: 27 February 2026 •
Published Online: 20 March 2026



Marko Cvejić,[1,a] Tal Queller,[1,b] Eyal Kroupp,[1] Dimitri Mikitchuk,[1,c] Ramy Doron,[1] Vladimir Bernshtam,[1] Oleg Nedostup,[1] Amnon Fruchtman,[2] and Yitzhak Maron[1]

## AFFILIATIONS

[1] Faculty of Physics, Weizmann Institute of Science, Rehovot 7610001, Israel
[2] Department of Physics, Holon Institute of Technology, Holon 58102, Israel

[a] **Author to whom correspondence should be addressed:** marko.cvejic@gmail.com
[b] **E-mail:** quellertal@gmail.com
[c] **Current address:** EPFL - Swiss Federal Technology Institute of Lausanne, Lausanne, Switzerland.

## ABSTRACT

We present a novel polarization-based spectroscopic method developed for measuring the radial component of the magnetic field, $B_r$, in an imploding magnetized-plasma column. The method is based on the combined effects of the Zeeman splitting and the Doppler shift. In the experiment, we use imploding oxygen plasma with a pre-embedded axial magnetic field $B_z$. Due to the axial non-uniformity of the plasma implosion and the field compression, the $B_z$ lines are bent radially. We measure the magnitude and direction of $\vec{B}$ along the radial coordinate; the magnitude is found to constitute a substantial fraction of the total $\vec{B}$ in the compressed plasma. The measurements extend the capabilities of spectroscopic diagnostics in magnetized plasmas, enabling a deeper understanding of the plasma dynamics (such as plasma rotation) and the energy flow in plasmas under high-current pulses.





## I. INTRODUCTION

Knowledge of the evolution of the magnetic field vector in experiments where high-energy-density plasmas (HEDP) are driven by pulsed high-current densities is essential for understanding the systems. Examples are Z-pinch implosions where the plasma is compressed by an azimuthal magnetic field $B_\theta$ (generated by the axial current density $J_z$). In such implosions an axial magnetic field $B_z$ can be applied initially to stabilize the implosion or to reduce thermal conduction, as considered for fusion.[1–8] In these experiments, the radially inward magnetic force due to $B_\theta$ is opposed by both the plasma pressure and the outward magnetic force due to $B_z$.

A notable phenomenon in Z-pinch experiments with an axial magnetic field $B_z$ is the bending of the compressed axial magnetic field near the axial boundaries of the Z-pinch implosions. Such curvatures of the compressed field may result either from the absence of the field compression in a metallic electrode (the field is frozen in the electrode), or from a slower plasma implosion near the electrodes. The bending of the initially applied axial magnetic field introduces a radial magnetic field component $B_r$, and possibly also a radial current density $J_r$ in certain $z$-locations. Importantly, such conditions give rise to an azimuthal magnetic force $F_\theta = J_z B_r - J_r B_z$. An illustration of the bending of the magnetic field near the electrodes is given in Fig. 1.

Indeed, experiments on gas-puff Z-pinches with an initially applied $B_z$, have shown that the curvature of the compressed $B_z$ near the electrodes can generate azimuthal forces, that lead to self-generated plasma rotation.[9] This rotation plays an important role in the energy balance and overall dynamics of the compressing cylindrical plasmas. Evidently, understanding the plasma rotation requires determining the various components of the magnetic field evolving throughout the plasma implosion.

The principal challenge in spectroscopic determination of magnetic fields in High-Energy-Density (HED) plasmas arises from the

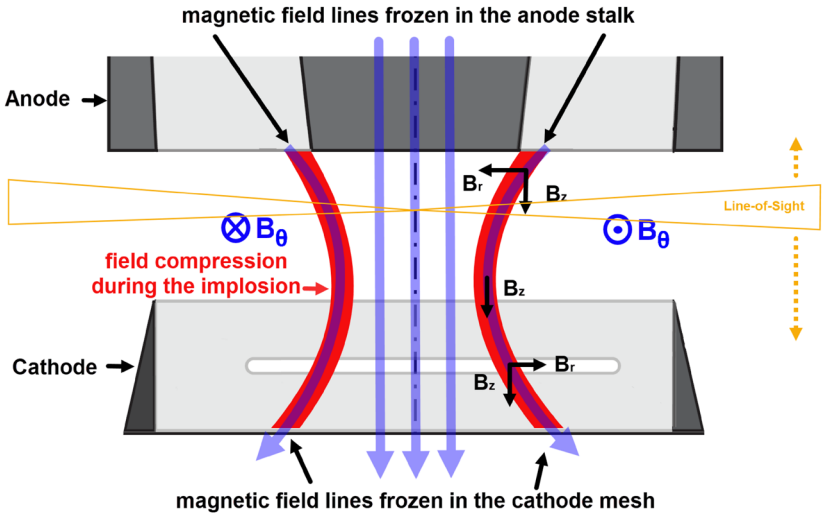


**FIG. 1.** Illustration of the magnetic field lines in the $[r, z]$ plane, showing the curvature close to the electrodes due to the compression. For more details about the geometry, see Fig. 2.

large widths of the spectral lines, which often preclude resolving the Zeeman pattern, formed due to the splitting of atomic levels into states with $m_j = -J, \ldots, J$ in the presence of a magnetic field. Alternative approaches to Zeeman spectroscopy are based on polarimetry,[10–14] or proton beam deflectometry.[15–17] Yet, extending the applicability of spectroscopic techniques to HED conditions is highly desirable, as they do not require an external probe beam. Since the spectral lines are broad, spectral resolution is not the limiting factor in resolving the Zeeman pattern. Instead, polarization-based methods, applicable when the magnetic field has a preferred spatial direction enable the field determination through simultaneous measurements of polarization-dependent differences in line shapes under a magnetic field.[9,18–26] A discussion of the capabilities of these methods is given in Ref. 27.

In Z-pinch implosions, such techniques have been used to measure the azimuthal magnetic field $B_\theta$[4,9,18–26,28] and the axial field $B_z$ in experiments where the compressed plasma was initially embedded with an axial field.[29] In these measurements, only the field magnitude was inferred, while the field direction was assumed. Here, we present a new spectroscopic method for determining the radial magnetic field component, $B_r$, which develops in a gas-puff Z-pinch experiment with an embedded $B_z$. The method utilizes the polarization properties of the Zeeman effect, together with the Doppler shifts arising from the radial implosion velocity.

The inferred $B_r$, found to be in the range of $\simeq 1-3T$, constitutes a substantial fraction of the total magnetic field ($\simeq 5-8T$). Combined with simultaneous measurements of $B_\theta$ and $B_z$, this technique enables the determination of both the magnitude and direction of $\vec{B}$, providing a significant step toward full vector magnetic field diagnostics in magnetized Z-pinch implosions and other cylindrically and spherically symmetric HED platforms.

## II. EXPERIMENTAL SETUP AND DIAGNOSTICS

Figure 2 shows schematics of the experimental setup, where a cylindrical oxygen-puff shell with an initial outer and inner radius of $R_{out}$ = 19 mm and $R_{in}$ = 7 mm, respectively, is injected via a fast valve into the anode-cathode (AK) gap through an annular de-Laval

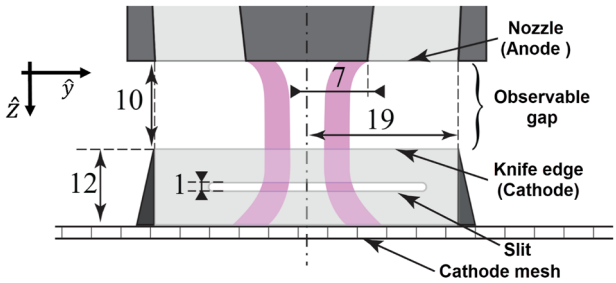


**FIG. 2.** $[r, z]$ plane of the experimental system. The spatial dimensions are in millimeters. $z = 0$ is the anode plane; $r = 0$ is the implosion axis; and $y$ is the projection of the radial axis on the ICCDs.

nozzle.[30] The linear mass density of the gas-load is $\approx 10\ \mu g/cm$, as determined by interferometry.[29] A pre-embedded, uniform, quasi-static axial magnetic field $B_z^0$, prefills the 10 mm A-K gap. $B_z^0$ is generated by a pair of Helmholtz Coils (HC), placed outside the vacuum chamber, carrying a current pulse of 95 ms rise-time allowing the diffusion of the magnetic field into the vacuum chamber and the A–K gap, yielding a magnetic field of $B_z^0 = 0.25 \pm 0.01\ T$, see Fig. 3.

A high-voltage discharge circuit, powered by a 25 kV – 16 $\mu$F capacitor bank, produces a current pulse peaking at 300 kA. The system self-inductance is $55nH$, which results in a pulse rise-time of 1.6 $\mu$s. The current at the time of the measurements is between 150 and 200 kA. The current pulse driven in the gas load generates and implodes the plasma together with the axial magnetic field. The time of the peak plasma compression (denoted by $t = 0$), is determined by the peak of a UV-visible photodiode signal that coincides with the minimum plasma radius observed in the 2D images. For the $B_z^0$ value used here, this occurs about 730 ns after the start of the current pulse. The cathode structure[9] consists of a cathode knife-edge (a 38 mm diameter metal cylinder) attached to a stainless-steel wire square mesh, with a wire diameter of 1 mm and a 5 mm-wide gap between the wires, as shown in Fig. 2. It was modified by adding

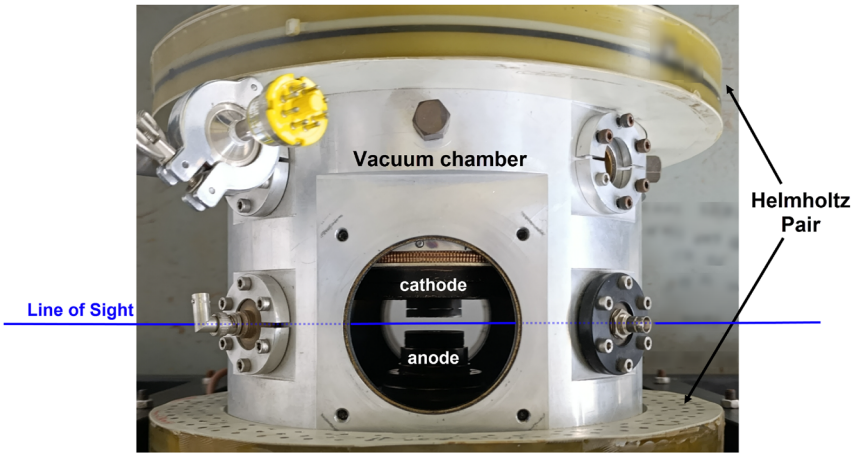


**FIG. 3.** Vacuum chamber and the A–K gap between the two Helmholtz coils.

a 1 mm-wide slit to its middle section around its circumference, as shown in Fig. 2. This modification enabled us diagnostic measurements of the cathode recess region without affecting the pinch dynamics.

Our diagnostics consist of UV-visible imaging spectroscopic system and a plasma-emission 2D imaging system. The spectroscopic system, shown in Fig. 4, employs polarization spectroscopy for measuring the combined effect of $B_r$ and $v_r$ on the line shape (see details in Sec. III) as well as the azimuthal B-field $B_\theta$. The imploding plasma column is observed side-on (including a cord along the diameter) at a specific $z$-position with an axial dimension $\Delta z = 0.66$ mm.

The optical design is illustrated in Fig. 4. The plasma emission from an $[r, \theta]$ plane (at a specific $z$-position) first passes through a quarter-wave plate that converts right- and left-circularly polarized emissions into two orthogonal linear polarizations that are subsequently separated into two beams using a polarizing beam splitter (PBS), which requires a sufficiently good alignment with the optical axis. Each beam is then focused onto one end of a bifurcated optical-fiber array, defining two polarization channels, denoted by RHCP and LHCP, each of which records one of the opposite circular polarizations of the Zeeman components, for a line of sight parallel to the $B$-field. The joint end of the array, carrying the Right-Hand Circular Polarization (RHCP) and Left-Hand Circular Polarization (LHCP) channels, is focused on the entrance slit of a 1 m spectrometer coupled to an Intensified Charge-Coupled Device (ICCD). The use of a single ICCD for the two channels ensures their synchronized recording.

The spectral resolution is 0.3 Å and the spatial resolution is 0.7 mm, while typical ICCD gate time is $\lesssim 30$ ns. This setup allows simultaneous measurement of emissions from the entire plasma column width (i.e., from $-y$ to $+y$) of both polarization channels on different parts of the same ICCD sensor, which improves accuracy in the determination of the spectral separation between the $\sigma_+$ and $\sigma_-$ Zeeman components. For the measurement of $B_r$ and $v_r$ (implosion velocity), we use the Line-of-Sight (LoS)

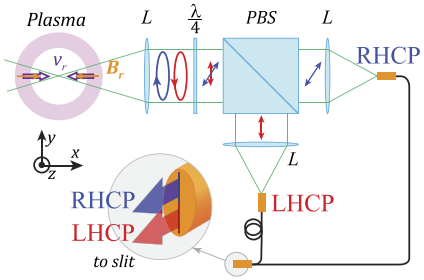


**FIG. 4.** Schematic description of the polarization spectroscopy system for the determination of $B_r$ and $v_r$. $\frac{\lambda}{4}$ is the quarter wave-plate; PBS is the polarizing beam-splitter; and L represents the lenses. RHCP and LHCP are the notation for the two different polarization direction channels.

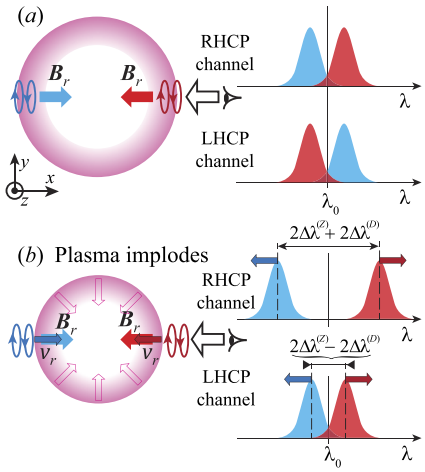


**FIG. 5.** Schematic description of the $B_r$ and $v_r$ measurement technique. The left panels depict a cross section of the plasma column, and the right panels present the corresponding measured line shapes in the RHCP and LHCP channels: (a) Assuming no implosion velocity and (b) assuming radial implosion velocity. The color of $v_r$ depicts its Doppler shift due to the implosion velocity: red to longer and blue to shorter wavelength. $2\Delta\lambda^{(Z)}$ is the peak separation (Zeeman splitting) caused by the magnetic field $B_r$, while $2\Delta\lambda^{(D)}$ is the peak separation (Doppler shifts) caused by the implosion $v_r$.

parallel to $B_r$, i.e., along the diameter at $y = 0$, shown in Figs. 4 and 5(a), while for the measurement of $B_\theta$ and $v_\theta$ (rotation velocity), we use the LoS that is parallel to $B_\theta$, i.e., along a cord at the outer plasma edge.[25] The imaging system is used for taking UV-visible, 5 ns gated images across the AK gap, simultaneously with the spectroscopic system. The LoS's of the spectroscopy and imaging systems are perpendicular to the pinch axis and to each other.

## III. MEASUREMENT METHOD

The measurement principle is illustrated in Fig. 5. In this work, we adopt the convention that the $\sigma_+$ Zeeman component is at a wavelength ($\lambda$) shorter than the unperturbed emission ($\lambda_0$). Since our side-on LoS simultaneously views regions where $B_r$ points toward and away from the observer, each Zeeman $\sigma$ component appears in both circular polarizations with the handedness interchanged between the two regions. Since the diagnostic system is sensitive to the polarization rotation direction, each polarization channel records both the $\sigma_+$ and $\sigma_-$ components. In particular, the RHCP channel records the $\sigma_+$ Zeeman component from $B_r$ directed toward the observer [the blue arrow and the blue spectral profile in Fig. 5(a)], as well as the $\sigma_-$ from $B_r$ directed away from the observer [the red arrow and the red spectral profile in Fig. 5(a)]. Conversely, the LHCP channel records the $\sigma_-$ and $\sigma_+$ components arising from $B_r$ directed toward and away from the observer, respectively.

In the absence of plasma motion (and assuming cylindrical symmetry), the RHCP and LHCP channels would record identical line profiles, each comprising two shifted $\sigma$ Zeeman components. Such spectral patterns cannot be used to determine $B_r$ since for the present plasma conditions and $B$-field magnitude, the Zeeman splitting is not large enough to provide reliable $B$ determination. However, due to the implosion, the Doppler shift causes the Zeeman components originating from the opposing $B$-fields to separate in opposite directions, as depicted in Fig. 5(b). In particular,

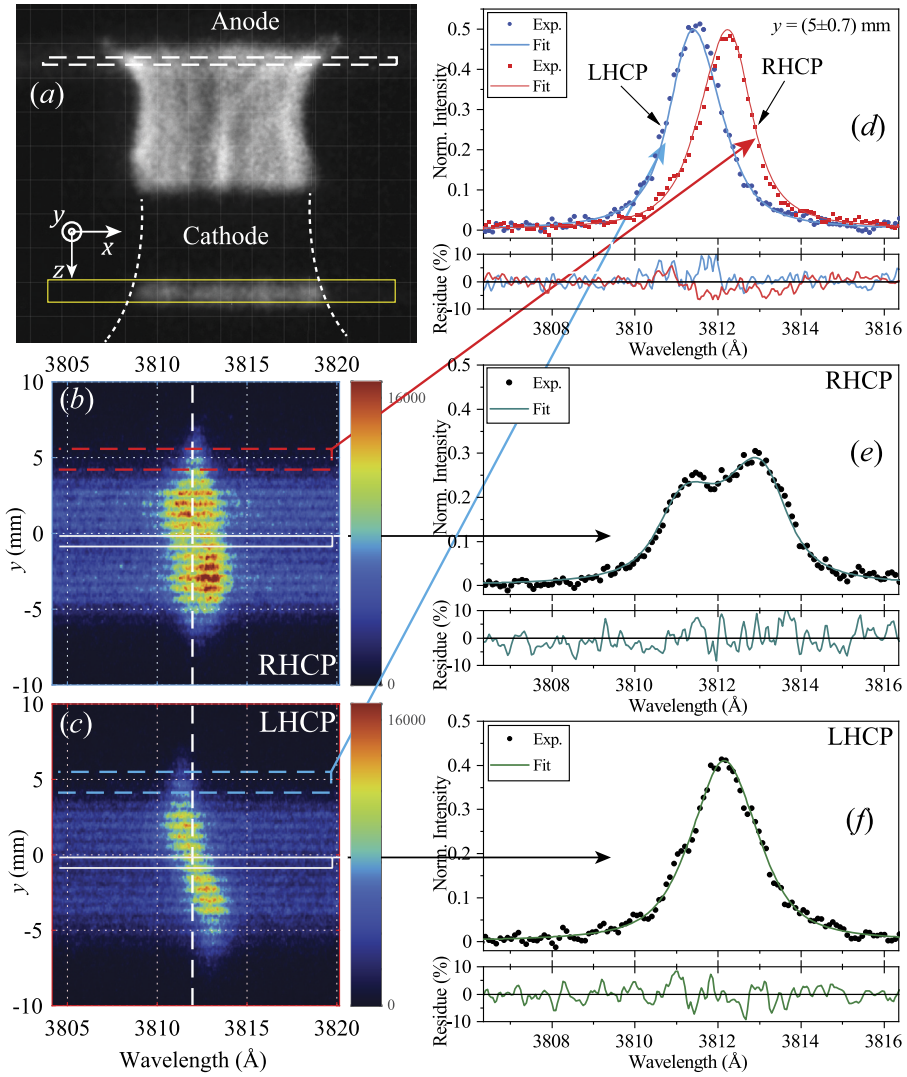


**FIG. 6.** (a) 2D self-emission image of the plasma at $t = -34$ ns. The $[y,\theta]$ plane projected on the spectrometer slit is depicted by the white dashed frame ($z = 1 \pm 0.3$ mm). The white dotted line indicates the plausible plasma shape within the cathode knife-edge, while the yellow rectangle indicates the slit opening cut through the cathode-knife edge. (b) The cordally integrated spectra of the *O VI* 3811.35 Å recorded on the RHCP channel. (c) Same as panel (b) for the LHCP channel. (d) The experimental lineouts at $y = 5 \pm 0.7$ mm from both the LHCP channel (blue dots) and the RHCP channel (red dots) with their best fits, used to determine $B_\theta$. (e) The lineout of the $y = 0 \pm 0.35$ mm cord on the RHCP channel (dots) and its best fit (cyan line) used to determine $B_r$ and $v_r$. The residue is shown on the lower panel. (f) The same as in panel (e) for the LHCP channel.

(i) in the RHCP channel, the Zeeman components shift away from each other, whereas (ii) in the LHCP channel, the components shift toward each other. The difference in line shapes between the RHCP and LHCP channels yields $B_r$ and $v_r$. While previous independent measurements along multiple azimuthal LoS's showed that the plasma implosion velocity is azimuthally symmetric to within 10%,[9] the method for determining $B_r$ remains applicable even in the absence of a symmetrical implosion. However, in this case, the line shape fitting will yield (in addition to $B_r$) the difference between the opposing radial velocities, rather than the absolute value of $v_r$. We note that the detection of similar emission intensities from the two sides of the LoS requires for the optical thinness of the transitions selected (CR computations give an opacity $\tau \approx 0.2$), which is consistent with the intensity ratio seen for the two doublet components. It is also worth noting that since we fit the entire line shape in order to get its peak position, our analysis is nearly unaffected by opacity.

## IV. MEASUREMENTS AND ANALYSIS

A typical measurement is presented in Fig. 6. The 2D plasma image, Fig. 6(a), shows the plasma shape late into the implosion, at $t = -34$ ns ($t = 0$ is defined at stagnation time), when the imploding plasma has bent the compressed axial magnetic field lines radially. The white dashed rectangle shows the region at $z = 1 \pm 0.3$ mm ($z = 0$ is the axial position of the anode edge), from which the radially resolved spectra of the *O VI* 3811.35 Å line, presented in Figs. 6(b) and 6(c), are recorded. These spectra correspond to the RHCP and LHCP polarization direction channels. Lineouts taken at $y = 0 \pm 0.3$ mm (along the diameter), shown in Figs. 6(e) and 6(f), exhibit noticeably different line shapes in the two recorded channels, consistent with the presence of $B_r$, during radial implosion, as illustrated in Fig. 5(b).

The determination of $B_r$ and $v_r$, as described in Sec. III, accounts for neither $B_\theta$ nor $B_z$. However, in our experiments, $B_\theta$ and $B_z$ are present at the same locations of $B_r$, i.e., the locations of radii corresponding to the O VI emission. It is important to note that for the LoS through $y = 0$, both $B_\theta$ and $B_z$ are perpendicular to the LoS, making their contribution to the Zeeman pattern indistinguishable. To resolve this ambiguity, we analyze spectral lineouts from the outer edge of the plasma shell (which is also the outer edge of O VI emission), where $B_\theta$ is parallel to the LoS;[20,25] see Fig. 6(d). In this location, $B_\theta$ is the dominant contributor to the Zeeman pattern (see Sec. IV B), namely, to the peak separation between the $\sigma_+$ and $\sigma_-$ components. Measuring $B_\theta$ separately facilitates the fitting of the recorded spectra, allowing the simultaneous determination of all three B-field components, $B_r, B_z$, and $B_\theta$. Here, we assume that $B_\theta$ is azimuthally symmetric, confirmed experimentally to within 15%. We note, however, that a lack of $B_\theta$ symmetry would not affect the applicability of the measurement method since $B_r$ could be determined from a single LoS at $y = 0$ (through the diameter), although in this case, it would not be possible to distinguish $B_z$ from $B_\theta$.

### A. Magnetic field determination

The analysis is based on the simultaneous fitting of the four spectral line shapes recorded in the two polarization direction channels RHCP and LHCP, from the two lineouts, (i) $y = 0 \pm 0.3$ mm and (ii) $y = 5 \pm 0.7$ mm, with the latter corresponding to the outer edge of the O VI plasma shell. A wider averaging range of ±0.7 mm is used for lineout from the edge in order to improve the signal-to-noise ratio. The experimental line shapes are Voigt, comprising a Lorentzian Stark broadening and a Gaussian component due to the spectral instrumental resolution (0.3 Å) and thermal Doppler broadening (0.23 Å), with the latter corresponding to an ion temperature of 10 eV, assuming thermal equilibrium between the O VI ion and the electrons (the electron temperature was previously

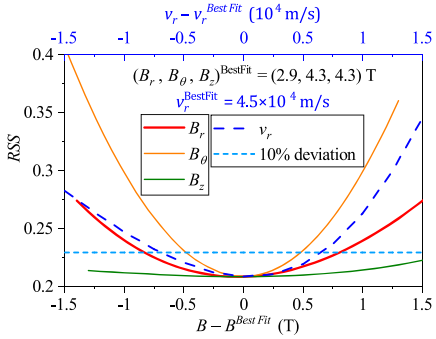


**FIG. 7.** RSS parameter used to describe the dependence of the quality of the fit on the parameters are in the bottom axis: $B_r$ (red line), $B\theta$ (orange line), and $B_z$ (green line) and the top axis: $v_r$ (blue dashed line) for the data in Fig. 6, $t = -34$ ns, $z = 1$ mm. The dotted blue line shows 10% deviation from the minimum RSS value, used here to determine the error bars of the best-fit values. Each curve only shows the dependence on one free parameter, while the others are fixed at their best-fit value.

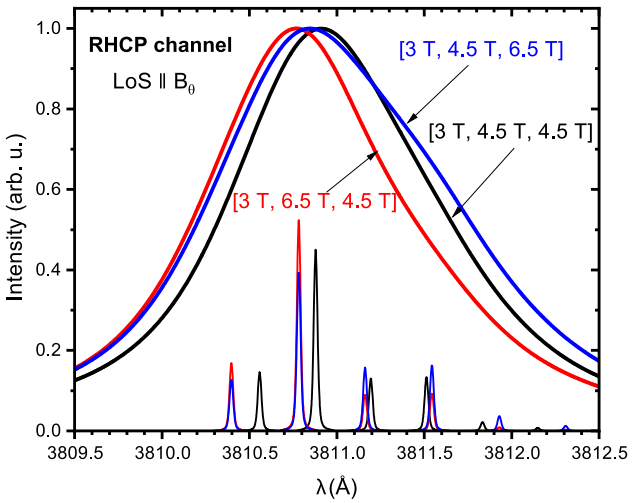


**FIG. 8.** Simulations of the *O VI* 3811.35 Å transition for various magnetic field vectors $[B_r, B_\theta, B_z]$, with a LoS parallel to $B_\theta$, illustrating the distinct effects of varying $B_\theta$ and $B_z$. The calculated Zeeman patterns (thin curves) are area-normalized to highlight the differences in the intensity distribution, while the convolved Voigt curves (0.3 Å Gaussian and 0.9 Å Lorentzian) are peak-normalized to emphasize the changes in the overall line shape and peak position. The polarization optics employed is included as in the simulations. For clarity, only the RHCP channel is shown.

determined[9]). The fitting of the recorded line shapes is carried out using the calculated Doppler-shifted Zeeman pattern convolved with Voigt profiles. The Lorentzian part $\omega_L$, due to Stark broadening, is a free fitting parameter from which the electron density ($n_e$) is obtained using Stark broadening parameters, as tabulated in Ref. 31.

In calculating the Zeeman pattern, we account for the angle between the LoS and the magnetic-field vector, composed of $B_r$, $B_\theta$, and $B_z$ (see the following paragraph). Doppler shifts are incorporated based on either the radial implosion velocity (for $y = 0$) or the rotational velocity (for $y = 5$ mm),[9] whereas the latter introduces identical Doppler shifts to both the RHCP and the LHCP channels and, therefore, does not affect the inferred magnetic fields. The simulations include the effects of the polarization optics, namely, the $\lambda/4$-plate and the PBS (see Fig. 4). Using Stokes vector parameterization[32] to describe the emission polarization state and Mueller matrices to represent the $\lambda/4$ plate and PBS, we calculate the effect of the optical components on the emitted photons. To determine the best-fit values, we performed simulations over a four-dimensional grid spanning various combinations of $B_r$, $B_\theta$, $B_z$, and $v_r$, enabling systematic comparison with the measured line shapes. To improve the computational efficiency, the grid was centered around the following initial estimates: $B_r^{start} = 3.2\ T$ and $v_r^{start} = 4.9 \times 10^4\ m/s$, obtained from the $y = 0$ lineout, neglecting the influence of $B_\theta$ and $B_z$ [as in Fig. 5(b)]; $B_\theta^{start} = 4.5\ T$ from the $y = 5$ mm lineout, neglecting the influence of $B_r$ and $B_z$ (as in Ref. 21). The initial $B_z^{start} = 3.7\ T$ was estimated by assuming an ideal, uniform flux compression within the imploding plasma shell. For each combination of $B$-field components and $v_r$, the Stark-Lorentzian width was fit independently. The fit quality was evaluated using the residual-sum-of-squares ($RSS$). The resulting $RSS$ values form a four-dimensional matrix dependent on $B_r$, $B_\theta$, $B_z$, and $v_r$. The best-fit corresponds to the set of magnetic field components and radial velocity yielding the minimum $RSS$. The resulting best-fit values for $z = 1$ mm, for example, are

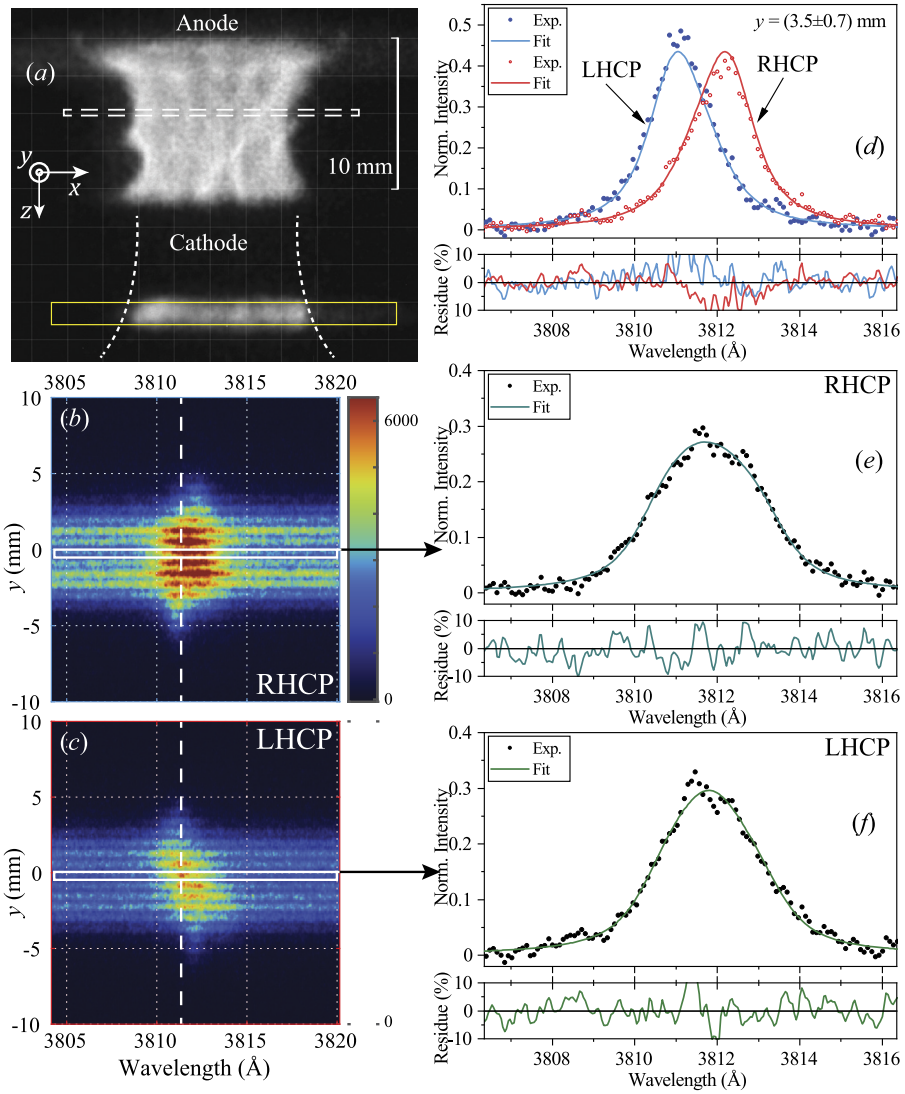


**FIG. 9.** (a) 2D self-emission image of the plasma at $t = -22$ ns. The $[r, \theta]$ plane projected on the spectrometer slit is depicted by the white dashed frame at $z = 4 \pm 0.3$ mm. The white dotted line shows the plausible plasma shape within the cathode knife-edge. (b) The cordally integrated spectra of the *O VI* 3811.35 Å line recorded on the RHCP channel. (c) The same as panel (b) for the LHCP channel. (d) The experimental lineouts at $y = 3.5 \pm 0.7$ mm from both the LHCP channel (blue dots) and the RHCP channel (red dots) with their best fits, used to determine $B\theta$. (e) The lineout of the $y = 0 \pm 0.35$ mm cord on the RHCP channel (dots) and its best fit (cyan line) used to determine $B_r$ and $v_r$. The residue is shown on the lower panel. (f) The same as in panel (e) for the LHCP channel.

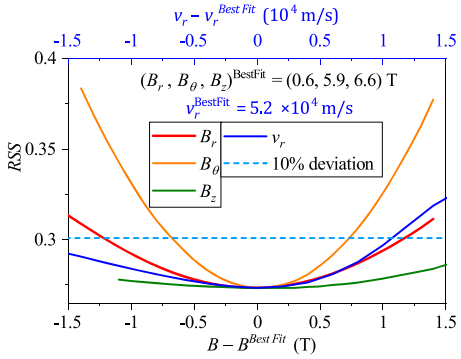


**FIG. 10.** RSS dependence on the free fitting parameters are in the bottom axis: $B_r$ (red line), $B_\theta$ (orange line), and $B_z$ (green line) and the top axis: $v_r$ (blue line) for the data in Fig. 9, $t = -22$ ns, $z = 4$ mm. The dotted blue line represents the 10% deviation of the minimum RSS value, used here to determine the error bars of the best-fit values. Each curve shows the dependence of only one free parameter while the others are fixed at their best-fit value.

(see Figs. 6(d)–6(f) and 7) $B_r = 2.9 \pm 0.8T$, $B_\theta = 4.3 \pm 0.5T$, $B_z = 4.3 \pm 1.6T$, and $v_r = 4.5 \pm 0.7 \times 10^4$ m$^2$/s. The line broadening is found to be Stark-dominated, with a fit Lorentzian width of 1.1 ± 0.25 Å, corresponding to $n_e = 1.1 \pm 0.25 \times 10^{18}$ cm$^{-3}$.

## B. Residual-sum-of-squares (*RSS*) dependence

The dependence of the *RSS* on $B_r$, $B_\theta$, $B_z$, and $v_r$ is shown in Fig. 7. The dotted line marks a 10% deviation from the minimum *RSS* value (the best fit), which is used to determine the error bars of the obtained values. This 10%-deviation criterion is chosen based on the examination of the deviations around the fitting results: simulations with *RSS* values exceeding this threshold exhibit significant discrepancies in both the overall line shapes and the positions of the peak intensities in the spectra compared to the experimental data. As usual, the steeper the *RSS* dependence on a certain parameter, the larger is its influence on the quality of the fit. For the present parameters, $B_\theta$ is found to carry the strongest effect, while the *RSS* sensitivities to $B_r$ and $v_r$, near their respective best-fit values, are

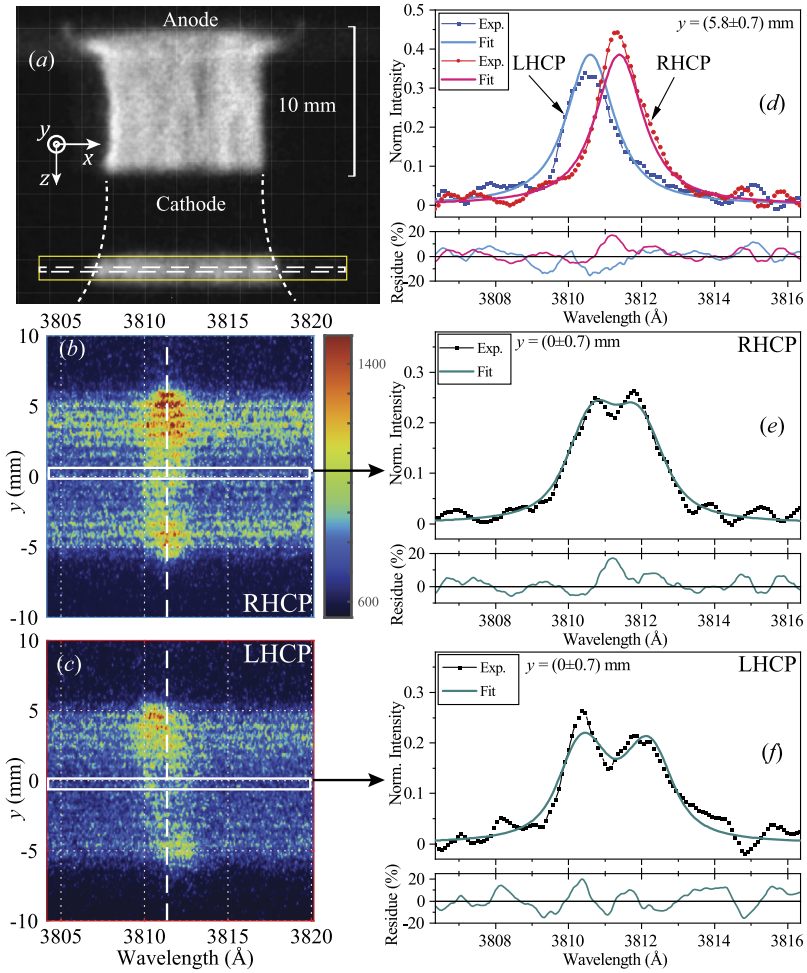


**FIG. 11.** (a) 2D self-emission image of the plasma at $t = -33$ ns. The $[r, \theta]$ plane projected on the spectrometer slit is depicted by the white dashed frame at $z = 15 \pm 0.3$ mm. The white dotted line indicates the plausible plasma shape within the cathode knife-edge. (b) The cordally integrated spectra of the *O VI* 3811.35 Å line recorded on the RHCP channel. (c) The same as panel (b) for the LHCP channel. (d) The experimental lineouts at $y = 4.7 \pm 0.7$ mm from both the LHCP channel (blue dots) and the RHCP channel (red dots) with their best fits, used to determine $B_\theta$. (e) The lineout of the $y = 0 \pm 0.35$ mm cord on the RHCP channel (dots) and its best fit (cyan line) used to determine $B_r$ and $v_r$. The residue is shown on the lower panel. (f) The same as in panel (e) for the LHCP channel.

similar. In addition, a large variation of $B_z$ has a negligible effect on the *RSS*.

The strong *RSS* dependence on $B_\theta$ can be understood as follows: as mentioned above, for the LoS $y = 0$, variations in $B_\theta$ and $B_z$, both perpendicular to the LoS, produce symmetric effects. Consequently, the stronger sensitivity to $B_\theta$ originates from the fits for $y = 5$ mm, where the LoS is parallel to $B_\theta$. For this LoS, the different effects of increasing $B_\theta$ vs increasing $B_z$ on the line shape are illustrated in Fig. 8. Increasing $B_\theta$ results in a larger splitting, with a Zeeman pattern closer to that of a LoS purely parallel to $B_\theta$, namely, dominated by the $\sigma$-Zeeman components. In contrast, increasing $B_z$ (instead of $B_\theta$), while producing the same total splitting (since the splitting depends on the magnitude $|B|$), results in a different intensity-distribution of the Zeeman pattern that affect the overall line shape less (compared to the effect due to an increased $B_\theta$). The same reasoning applies when either $B_\theta$ or $B_z$ are weaker.

Variations in $B_r$ (via the fits to the LoS for $y = 0$) should qualitatively show a similar effect to variations in $B_\theta$, but their influence on the *RSS* is weaker, simply due to the lower magnitude of $B_r$.

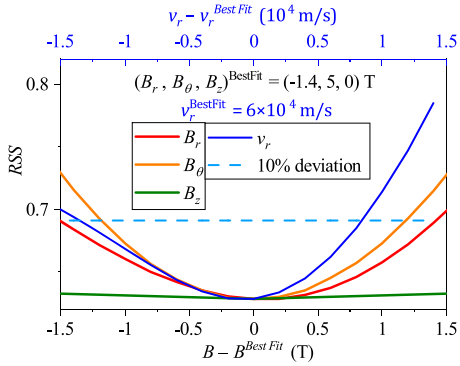


**FIG. 12.** RSS dependence on the free fitting parameters are in the bottom axis: $B_r$ (red line), $B_\theta$ (orange line), and $B_z$ (green line) and the top axis: $v_r$ (blue line) for the data in Fig. 11, $t = -33$ ns, $z = 15$ mm. The dotted blue line represents the 10% deviation of the minimum RSS value, used here to determine the error bars of the best-fit values. Each curve shows the dependence of only one free parameter while the others are fixed at their best-fit value.

### C. Dependence of $B_r$ on the axial location

The thickness of the *O VI* emission shell is between $d = 1$ and 1.5 mm at $t > -50$ ns at all $z$-locations. The outer radius of the *O VI* charge state, defined as the position of half-peak emission as it diminishes toward larger radii, coincides with the outer plasma radius $r_{plasma}$, which is determined by the half-peak intensity in the imaging. Since $B_r$ is measured using the *O VI* transition, the radius at which $B_r$ is obtained corresponds to $r_{plasma}$. As seen from the 2D plasma images in Fig. 6(a), the plasma radius varies with $z$. We assume qualitatively that the curvature of $B$ in $[r, z]$ is similar to that of the plasma. This curvature is defined by the angle between the plasma-vacuum boundary tangent [at $r_{plasma}(z)$] and the plasma axis, i.e., $\alpha = \arctan\frac{\Delta r}{\Delta z}$. As shown in the plasma images [Fig. 6(a) and Fig. 11(a)], the plasma curvature is most pronounced near the anode ($z \approx 0$). At $z = 1$ mm, the outer plasma radius is $r_{plasma} = 6.5$ mm, while at $z = 4$ mm, it decreases to $r_{plasma} = 5.2$ mm. Consequently, we expect that $|B_r|(z = 4\text{ mm}) < |B_r|(z = 1\text{ mm})$. In Figs. 9 and 10, we present the measurements and analysis for $z = 4$ mm at $t = -22$ ns. Indeed, $B_r(z = 4) = 0.6 \pm 1.1T$, compared to $B_r(z = 1) = 2.9 \pm 0.8T$. The larger error bar for $B_r(z = 4\text{ mm})$ is due to the increased Stark broadening caused by a higher plasma density close to stagnation. Although the measurement at $z = 4$ mm was made at a later time, the plasma curvature at this location ($\alpha \leq 10^\circ$) remains approximately the same for both instances, justifying the comparison. As mentioned before, the cathode structure consists of a cathode-knife edge (a 38 mm diameter metal cylinder) attached to a stainless-steel wire square mesh, with a wire diameter of 1 mm and a 5 mm-wide gap between the wires, as shown in Fig. 2. In order to perform measurements within the hollow cathode-structure, we use a LoS through a slit cut in the cathode cylinder at $z = 15$ mm, namely, 6 mm from the cathode metallic mesh, as shown in Fig. 2. At this location, a curvature of the compressed magnetic field lines near the cathode is expected to be found at least in part due to the field tying to the multiple mesh wires, as the skin depth of the *B*-field in the wires over the implosion timescale is comparable with the wire diameter. Indeed, at this location, we observe a slower plasma compression, as presented in Figs. 6(a), 9(a), and 11(a). It is seen that at $z = 15$ mm, the plasma radius is $r_{plasma}(z = 15) = 6$ mm, larger than $r_{plasma}(z = 4) = 5.2$ mm. Evidently, given the observed plasma curvature near the cathode and the $B_z$ orientation (directed from the anode to the cathode), the expected direction of $B_r$ near the cathode is outward, opposite to that near the anode. Opposite direction of $B_r$ should lead to a broader line shape in the LHCP channel (see Sec. III). Indeed, the measured line shapes at $z = 15$ mm at $t = -33$ ns, shown in Figs. 11 and 12, display a broader profile in the LHCP channel, confirming the expected reversal of $B_r$. Analysis of the data yields $B_r = -1.4 \pm 1.4T$.

## V. DISCUSSION

As mentioned above, the compression of the plasma and of the embedded axial magnetic field is usually non-uniform due to the common slower implosion and slower field compression near the Z-pinch edges, namely, the anode and the cathode structures. The resulting curvature in the compressed field lines forms a radial component for the compressed field. In our gas-puff Z-pinch, the main reason for the curvature of $\vec{B}$ near the anode and cathode is, respectively, the freezing of the B-field in the metallic anode and in the wire mesh in the cathode structure. The mutual interaction between the compressing plasma and B-field causes the plasma to develop a spatial shape that is similar to the compressed field lines, both near the anode and the cathode, as can be seen by the plasma imaging; see Figs. 6(a), 9(a), and 11(a). The similarity of the spatial curvature is consistent with the estimated magnetic Reynolds number $R_m$, defined as $R_m = \mu_0\sigma_0 v_r L$, where $\sigma_0$ is the plasma conductivity and $L \approx 2$ mm is the plasma shell thickness. Using the Spitzer conductivity for our experimental conditions ($T_e \approx 10 - 12$ eV) and the measured radial velocity $v_r \approx 5 - 7 \times 10^4 m^2/s$, we find $R_m \approx 8 - 12$, indicating that the magnetic-field diffusion velocity is about 10 times lower than the flow velocity. Indeed, due to the field curvature, we measure $B_r = 2.9 \pm 0.8T$ near the anode ($z = 1$ mm) and $B_r = -1.4 \pm 1.4T$ inside the cathode ($z = 15$ mm), as shown in Figs. 6 and 11, respectively, and Table I.

**TABLE I.** $B_r$ dependence on $z$-locations, where $z = 0$ is the plane of the anode edge (gas-puff nozzle), $z = 10$ mm is the plane of the cathode knife-edge, and $z = 15$ mm is the plane of the middle of the slit cut in the cathode knife-edge; see Fig. 2. The radius column indicates the radius at which $B_r$ is measured and the error bar.

| z-position (mm) | Radius (mm) | $B_r$ $(T)$ |
|---|---|---|
| 1 ± 0.3 | 6 ± 1 | 2.9 ± 0.8 |
| 4 ± 0.3 | 4.7 ± 1 | 0.6 ± 1.1 |
| 15 ± 0.3 | 5.5 ± 1 | −1.4 ± 1.4 |

The plasma imaging in the present work is performed along a LoS perpendicular to that of the spectroscopic diagnostics, used for the determination of $B_r$. Thus, the data can be used to quantitatively analyze the correlation between plasma shape curvature and the orientation of the $B$-field vector. This analysis will be presented in a separate publication, aided by more observations of both $B_r$ and the plasma shape within the hollow cathode-volume.

We note that the presence of $B_r$, as observed, does not necessarily cause net azimuthal forces in the plasma since, in principle, the current and magnetic field can be parallel to each other in the $(z, r)$ plane $[\vec{J} \times \vec{B}]_\theta = 0$. However, in our experiment, azimuthal forces are present, based on the self-generated plasma rotation observed.[9] The rotation velocity was found to be comparable with the peak implosion velocity, significantly affecting the radial force balance, and the rotation direction was found to reverse for an opposite direction of ${B^0}_z$. The measurements of $B_r$ presented in this work are thus crucial for understanding the plasma rotation, caused by the $j_z B_r$ and $j_r B_z$ forces.

Determining $j_r(r)$ requires measuring $B_\theta(r, z)$ since $j_r \approx \frac{\partial B\theta}{\partial z}$, which will be addressed in future work. To understand the observed $r$ dependence of the rotation,[9] $B_r$ and $j_r$ must be measured simultaneously at different radii, which can be achieved by utilizing the emission shape of transitions of multiple charge states, residing in different radii, in a single discharge.[9,19,21]

In summary, using a newly developed spectroscopic method that utilizes the combined effects of the Zeeman splitting and the Doppler shifts due to the plasma motion, we measured the radial component of the magnetic field. The measurement method, data analysis, and limitations were demonstrated on cylindrical imploding gas-puff plasma. These have potential applications in HEDP diagnostics, for which there is a magnetic field projection along the LoS and the plasmas move in opposite directions along the same LoS. Such experiments can be those of plasma jets simulating astrophysical phenomena,[33–35] magnetic reconnection experiments,[36–38] differentially rotating plasmas,[39] and pulsed magnetic mirror fields with wire array Z-pinches.[40] Furthermore, combining such measurements, with the simultaneous measurements of other $b$-field components[9,19–22,25,26,29] can be of high significance in broader HEDP experiments.

## ACKNOWLEDGMENTS

We thank Tal Rubin, Mike Mlodik, and Nat Fisch for invaluable discussions on the plasma rotation. We thank Simon Bland, Sergey Lebedev, and Lee Suttle for illuminating discussions on the present experiment and on their future HEDP experiments. The authors thank Pesah Meiri for technical assistance. This work was supported in part by the University of Michigan Multi-University Center of Excellence for Magnetic Acceleration, Compression, and Heating (U.S.), Sandia National Laboratories (U.S.), Lawrence Livermore National Laboratory (U.S.), the Israeli Institute for Fusion Research and the Israeli Ministry of Energy, the US-Israel BSF-NSF Foundation, and by the UK-WIS Making Connections grant.

## AUTHOR DECLARATIONS

### Conflict of Interest

The authors have no conflicts to disclose.

### Author Contributions

**Marko Cvejić**: Conceptualization (equal); Data curation (equal); Formal analysis (equal); Methodology (equal); Writing – original draft (equal); Writing – review & editing (equal). **Tal Queller**: Conceptualization (equal); Data curation (equal); Formal analysis (equal); Investigation (equal); Methodology (equal); Writing – original draft (equal); Writing – review & editing (equal). **Eyal Kroupp**: Conceptualization (equal); Data curation (supporting); Investigation (equal); Methodology (equal); Supervision (equal); Validation (equal); Writing – review & editing (equal). **Dimitri Mikitchuk**: Conceptualization (equal); Formal analysis (equal); Software (equal); Writing – original draft (equal). **Ramy Doron**: Methodology (equal); Software (supporting); Writing – review & editing (equal). **Vladimir Bernshtam**: Investigation (equal); Resources (equal); Software (supporting). **Oleg Nedostup**: Investigation (equal); Resources (equal); Software (supporting). **Amnon Fruchtman**: Supervision (supporting); Validation (lead); Visualization (supporting); Writing – review & editing (supporting). **Yitzhak Maron**: Conceptualization (supporting); Investigation (supporting); Methodology (supporting); Project administration (lead); Resources (lead); Supervision (lead); Validation (lead); Visualization (supporting); Writing – review & editing (lead).

## DATA AVAILABILITY

The data that support the findings of this study are available from the corresponding author upon reasonable request.

## REFERENCES

[1] S. A. Slutz, M. C. Herrmann, R. A. Vesey, A. B. Sefkow, D. B. Sinars, D. C. Rovang, K. J. Peterson, and M. E. Cuneo, Phys. Plasmas **17**, 056303 (2010).
[2] S. A. Slutz and R. A. Vesey, Phys. Rev. Lett. **108**, 025003 (2012).
[3] M. E. Cuneo, M. C. Herrmann, D. B. Sinars, S. A. Slutz, W. A. Stygar, R. A. Vesey, A. B. Sefkow, G. A. Rochau, G. A. Chandler, J. E. Bailey, J. L. Porter, R. D. McBride, D. C. Rovang, M. G. Mazarakis, E. P. Yu, D. C. Lamppa, K. J. Peterson, C. Nakhleh, S. B. Hansen, A. J. Lopez, M. E. Savage, C. A. Jennings, M. R. Martin, R. W. Lemke, B. W. Atherton, I. C. Smith, P. K. Rambo, M. Jones, M. R. Lopez, P. J. Christenson, M. A. Sweeney, B. Jones, L. A. McPherson, E. Harding, M. R. Gomez, P. F. Knapp, T. J. Awe, R. J. Leeper, C. L. Ruiz, G. W. Cooper, K. D. Hahn, J. McKenney, A. C. Owen, G. R. McKee, G. T. Leifeste, D. J. Ampleford, E. M. Waisman, A. Harvey-Thompson, R. J. Kaye, M. H. Hess, S. E. Rosenthal, and M. K. Matzen, IEEE Trans. Plasma Sci. **40**, 3222 (2012).
[4] M. R. Gomez, S. A. Slutz, A. B. Sefkow, D. B. Sinars, K. D. Hahn, S. B. Hansen, E. C. Harding, P. F. Knapp, P. F. Schmit, C. A. Jennings, T. J. Awe, M. Geissel, D. C. Rovang, G. A. Chandler, G. W. Cooper, M. E. Cuneo, A. J. Harvey-Thompson, M. C. Herrmann, M. H. Hess, O. Johns, D. C. Lamppa, M. R. Martin, R. D. McBride, K. J. Peterson, J. L. Porter, G. K. Robertson, G. A. Rochau, C. L. Ruiz, M. E. Savage, I. C. Smith, W. A. Stygar, and R. A. Vesey, Phys. Rev. Lett. **113**, 155003 (2014).

[5]A. B. Sefkow, S. A. Slutz, J. M. Koning, M. M. Marinak, K. J. Peterson, D. B. Sinars, and R. A. Vesey, Phys. Plasmas **21**, 072711 (2014).
[6]D. A. Yager-Elorriaga, M. R. Gomez, D. E. Ruiz, S. A. Slutz, A. J. Harvey-Thompson, C. A. Jennings, P. F. Knapp, P. F. Schmit, M. R. Weis, T. J. Awe, G. A. Chandler, M. Mangan, C. E. Myers, J. R. Fein, B. R. Galloway, M. Geissel, M. E. Glinsky, S. B. Hansen, E. C. Harding, D. C. Lamppa, W. E. Lewis, P. K. Rambo, G. K. Robertson, M. E. Savage, G. A. Shipley, I. C. Smith, J. Schwarz, D. J. Ampleford, K. Beckwith, K. J. Peterson, J. L. Porter, G. A. Rochau, and D. B. Sinars, Nucl. Fusion **62**, 042015 (2022).
[7]A. J. Harvey-Thompson, M. E. Geissel, W. E. Lewis, D. A. Yager-Elorriaga, M. R. Weis, C. A. Jennings, J. R. Fein, D. J. Ampleford, M. R. Gomez, E. C. Harding, S. B. Hansen, D. E. Bliss, G. A. Chandler, G. S. Dunham, E. S. Field, B. R. Galloway, M. Glinsky, K. D. Hahn, P. F. Knapp, D. C. Lamppa, L. M. Lucero, M. A. Mangan, R. R. Paguio, L. Perea, K. J. Peterson, J. L. Porter, P. K. Rambo, G. K. Robertson, G. A. Rochau, D. E. Ruiz, C. L. Ruiz, M. A. Schaeuble, J. Schwarz, J. E. Shores, D. B. Sinars, S. A. Slutz, G. E. Smith, I. C. Smith, C. S. Speas, K. Whittemore, and E. P. Yu, Phys. Plasmas **31**, 072711 (2024).
[8]D. J. Ampleford, D. A. Yager-Elorriaga, C. A. Jennings, E. C. Harding, M. R. Gomez, A. J. Harvey-Thompson, T. J. Awe, G. A. Chandler, G. S. Dunham, M. Geissel, K. D. Hahn, S. B. Hansen, P. F. Knapp, D. C. Lamppa, W. E. Lewis, L. Lucero, M. Mangan, R. Paguio, L. Perea, G. A. Robertson, C. L. Ruiz, D. E. Ruiz, P. F. Schmit, S. A. Slutz, G. E. Smith, I. C. Smith, C. S. Speas, T. J. Webb, M. R. Weis, K. Whittemore, E. P. Yu, R. D. McBride, K. J. Peterson, B. M. Jones, G. A. Rochau, and D. B. Sinars, Phys. Plasmas **31**, 022703 (2024).
[9]M. Cvejić, D. Mikitchuk, E. Kroupp, R. Doron, P. Sharma, Y. Maron, A. L. Velikovich, A. Fruchtman, I. E. Ochs, E. J. Kolmes, and N. J. Fisch, Phys. Rev. Lett. **128**, 015001 (2022).
[10]J. A. Stamper and B. H. Ripin, Phys. Rev. Lett. **34**, 138 (1975).
[11]M. Borghesi, A. J. MacKinnon, A. R. Bell, R. Gaillard, and O. Willi, Phys. Rev. Lett. **81**, 112 (1998).
[12]M. Tatarakis, I. Watts, F. N. Beg, E. L. Clark, A. E. Dangor, A. Gopal, M. G. Haines, P. A. Norreys, U. Wagner, M.-S. Wei, M. Zepf, and K. Krushelnick, Nature **415**, 280 (2002).
[13]S. N. Bland, D. J. Ampleford, S. C. Bott, A. Guite, G. N. Hall, S. M. Hardy, S. V. Lebedev, P. Shardlow, A. Harvey-Thompson, F. Suzuki, and K. H. Kwek, Rev. Sci. Instrum. **77**, 10E315 (2006).
[14]V. V. Ivanov, A. A. Anderson, D. Papp, A. L. Astanovitskiy, B. R. Talbot, J. P. Chittenden, and N. Niasse, Phys. Rev. E **88**, 013108 (2013).
[15]C. K. Li, F. H. Séguin, J. A. Frenje, J. R. Rygg, R. D. Petrasso, R. P. J. Town, P. A. Amendt, S. P. Hatchett, O. L. Landen, A. J. Mackinnon, P. K. Patel, V. A. Smalyuk, T. C. Sangster, and J. P. Knauer, Phys. Rev. Lett. **97**, 135003 (2006).
[16]P. M. Nilson, L. Willingale, M. C. Kaluza, C. Kamperidis, S. Minardi, M. S. Wei, P. Fernandes, M. Notley, S. Bandyopadhyay, M. Sherlock, R. J. Kingham, M. Tatarakis, Z. Najmudin, W. Rozmus, R. G. Evans, M. G. Haines, A. E. Dangor, and K. Krushelnick, Phys. Plasmas **15**, 092701 (2008).
[17]N. L. Kugland, D. D. Ryutov, C. Plechaty, J. S. Ross, and H.-S. Park, Rev. Sci. Instrum. **83**, 101301 (2012).
[18]R. P. Golingo, U. Shumlak, and D. J. Den Hartog, Rev. Sci. Instrum. **81**, 126104 (2010).
[19]G. Rosenzweig, E. Kroupp, A. Fisher, and Y. Maron, J. Instrum. **12**, P09004 (2017).
[20]D. Mikitchuk, M. Cvejić, R. Doron, E. Kroupp, C. Stollberg, Y. Maron, A. L. Velikovich, N. D. Ouart, J. L. Giuliani, T. A. Mehlhorn, E. P. Yu, and A. Fruchtman, Phys. Rev. Lett. **122**, 045001 (2019).
[21]G. Rosenzweig, E. Kroupp, T. Queller, A. Starobinets, Y. Maron, V. Tangri, J. L. Giuliani, and A. Fruchtman, Phys. Plasmas **27**, 022705 (2020).
[22]Y. Maron, Phys. Plasmas **27**, 060901 (2020).
[23]N. Aybar, M. Dozieres, D. B. Reisman, M. Cvejić, D. Mikitchuk, F. Conti, E. Kroupp, R. Doron, Y. Maron, and F. N. Beg, Phys. Rev. E **103**, 053205 (2021).
[24]N. A. Aybar, F. Conti, M. Cvejić, D. Mikitchuk, M. Dozières, E. Kroupp, J. Narkis, Y. Maron, and F. N. Beg, IEEE Trans. Plasma Sci. **50**, 2541 (2022).
[25]Y. Maron, R. Doron, M. Cvejić, E. Stambulchik, D. Mikitchuk, C. Stollberg, T. Queller, E. Kroupp, G. Rosenzweig, B. Rubinstein, S. Biswas, V. Bernshtam, O. Nedostup, V. Litmanovich, V. Fisher, A. Starobinets, A. Fruchtman, A. Fisher, V. Tangri, J. L. Giuliani, A. L. Velikovich, A. Dasgupta, I. E. Ochs, E. J. Kolmes, M. E. Mlodik, S. Davidovits, N. J. Fisch, and M. D. Johnston, IEEE Trans. Plasma Sci. **51**, 3407 (2023).
[26]C. Stollberg, E. Kroupp, D. Mikitchuk, P. Sharma, V. Bernshtam, M. Cvejić, R. Doron, E. Stambulchik, Y. Maron, A. Fruchtman, I. E. Ochs, N. J. Fisch, and U. Shumlak, Phys. Rev. Lett. **130**, 205101 (2023).
[27]R. Doron, D. Mikitchuk, C. Stollberg, G. Rosenzweig, E. Stambulchik, E. Kroupp, Y. Maron, and D. A. Hammer, High Energy Density Phys. **10**, 56 (2014).
[28]G. Davara, L. Gregorian, E. Kroupp, and Y. Maron, Phys. Plasmas **5**, 1068 (1998).
[29]D. Mikitchuk, *Investigation of the Compression of Magnetized Plasma and Magnetic Flux* (Springer Cham, 2019).
[30]D. B. Atkinson and M. A. Smith, Rev. Sci. Instrum. **66**, 4434 (1995).
[31]N. M. S. Sahal-Bréchot and M. S. Dimitrijević, Stark-B Database [online], Observatory of Paris, Lerma and Astronomical Observatory of Belgrade (2020).
[32]W. H. McMaster, Am. J. Phys. **22**, 351 (1954).
[33]F. Suzuki-Vidal, S. V. Lebedev, S. N. Bland, G. N. Hall, A. J. Harvey-Thompson, J. P. Chittenden, A. Marocchino, S. C. Bott, J. Palmer, and A. Ciardi, IEEE Trans. Plasma Sci. **38**, 581 (2010).
[34]T. Byvank, J. T. Banasek, W. M. Potter, J. B. Greenly, C. E. Seyler, and B. R. Kusse, Phys. Plasmas **24**, 122701 (2017).
[35]E. S. Lavine, D. A. Lund, E. Freeman, W. M. Potter, C. E. Seyler, and B. R. Kusse, Phys. Plasmas **32**, 012902 (2025).
[36]J. D. Hare, L. Suttle, S. V. Lebedev, N. F. Loureiro, A. Ciardi, G. C. Burdiak, J. P. Chittenden, T. Clayson, C. Garcia, N. Niasse, T. Robinson, R. A. Smith, N. Stuart, F. Suzuki-Vidal, G. F. Swadling, J. Ma, J. Wu, and Q. Yang, Phys. Rev. Lett. **118**, 085001 (2017).
[37]R. Datta, K. Chandler, C. E. Myers, J. P. Chittenden, A. J. Crilly, C. Aragon, D. J. Ampleford, J. T. Banasek, A. Edens, W. R. Fox, S. B. Hansen, E. C. Harding, C. A. Jennings, H. Ji, C. C. Kuranz, S. V. Lebedev, Q. Looker, S. G. Patel, A. Porwitzky, G. A. Shipley, D. A. Uzdensky, D. A. Yager-Elorriaga, and J. D. Hare, Phys. Rev. Lett. **132**, 155102 (2024).
[38]T. W. O. Varnish, J. Chen, S. Chowdhry, R. Datta, G. V. Dowhan, L. S. Horan, IV, N. M. Jordan, E. R. Neill, A. P. Shah, R. Shapovalov, B. J. Sporer, R. D. McBride, and J. D. Hare, Phys. Plasmas **32**, 022118 (2025).
[39]V. Valenzuela-Villaseca, L. G. Suttle, F. Suzuki-Vidal, J. W. D. Halliday, S. Merlini, D. R. Russell, E. R. Tubman, J. D. Hare, J. P. Chittenden, M. E. Koepke, E. G. Blackman, and S. V. Lebedev, Phys. Rev. Lett. **130**, 195101 (2023).
[40]C. Chen, E. S. Lavine, W. M. Potter, C. E. Seyler, and B. R. Kusse, Phys. Plasmas **31**, 072704 (2024).